Simulation of a helicopter rotor flow

Juho Ilkko, Jaakko Hoffren and Timo Siikonen

Summary. Flowfield around the isolated main rotor of UH-60A helicopter was simulated to validate flow solver FINFLO for rotary wing applications. The computational model treated the four blades as rigid but hinged at their roots, and their dynamic movements resulting from the blade angle controls were solved interactively with the time-accurate flow solution that applies Reynolds-averaged Navier-Stokes equations. A hover case and a fast flight forward were studied with an overset grid system having around 20 million cells. With approximate modeling of appreciable blade elastic torsion, quite good agreement with the experimental and computational data taken from the literature was achieved.

Key words: helicopter rotor flow, CFD, fluid-structure interaction, multi-body dynamics

Introduction

Helicopters utilize rotating airfoils, i.e. rotors, instead of fixed wings to produce the necessary lift. The principle involves interconnected aerodynamic, mechanical and structural problems that must be sufficiently well understood to design, produce and maintain a successful helicopter. For example, even simple repairs of rotor blades must be conducted with extreme care, because they may locally modify the delicate mass and stiffness distributions, potentially producing serious extra vibrations or reduction of the rotor fatigue life. To predict the effects of rotor variations, sophisticated computational simulations are needed.

Comprehensive rotor simulations have been applied especially in the US since the advent of sufficiently powerful computers [1],[2],[3],[4]. Various software packages have been incrementally developed over the years. Typically, these codes contain non-linear models of the rotor mechanics and structure, whereas the aerodynamic modeling has traditionally been based on a time-dependent potential flow theory. Over the past decades, flow models based on time-accurate numerical solutions of Navier-Stokes equations have begun to supersede the simpler, less realistic models. In addition to the simulations, there have been some extensive experimental campaigns to actually measure the operation of helicopter rotors both in wind tunnels and even in flight [5],[6],[7] to obtain reference data for validation. Results from the computational and experimental studies as well as from their comparisons have been published, but there is actually a very limited amount of detailed data publicly available to support the independent development of rotor simulations.

In this paper, recent work on the development of rotor simulations in Finland is described. The main emphasis is on aerodynamics modeling based on the Navier-Stokes equations and on validation of the FINFLO flow solver [8]. Firstly, some background on helicopter technology is given to understand the simulation of the fluid-structure interaction and the inherent problems. The subsequent description of the computational model

includes the mechanical and flow models. Computational results for the main rotor of a Sikorsky UH-60A helicopter are then compared with available references.

Aeromechanics of helicopter rotor

Helicopter main forces

The distinctive main component of a typical helicopter is the single main rotor that acts like a large propeller. The main rotor combines the production of lift to overcome the weight of the helicopter W and that of propulsive force in the direction of flight to overcome the drag D. In addition, the control of the helicopter is accomplished mainly through control of the rotor. The idea is to set the magnitude and direction of the total thrust vector T produced by the rotor so that the desired state of flight at flying speed V is realized, as illustrated in Fig. 1. In its operation, the main rotor corresponds to the combination of the wings, propulsion system and tailplane of a fixed-wing aircraft. In the following, the operation of a multi-bladed rotor is described.
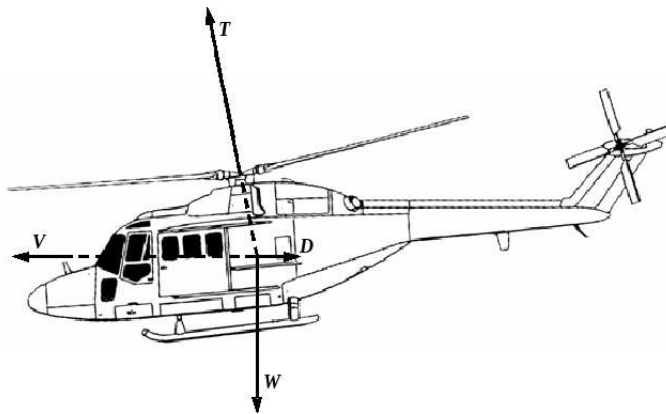

Figure 1. Main forces W, T and D of a helicopter in level flight at velocity V.

Blade motions and hinges

A hover or vertical flight is the simplest operating state of a rotor. The rotor thrust is directed downwards, and its magnitude is controlled by changing the blade angles $\boldsymbol{\theta}$, i.e. by adjusting them about a longitudinal or feathering axis along each blade, shown in Fig. 2. The rotor angular speed $\boldsymbol{\Omega}$ is always kept essentially constant in flight because of the great inertia involved.

To tilt the thrust vector for forward flight, the helicopter pilot adjusts the blade angles cyclically, dependent on the blade position $\boldsymbol{\Psi} = \boldsymbol{\Omega}t$ varying with time t. A plane defined by the paths of the blade tips must also tilt forward, because the thrust vector of a rotor is always essentially perpendicular to this tip plane, as indicated by Fig. 1. The change in the thrust vector produces a horizontal force component that accelerates the helicopter until the increasing drag leads to an equilibrium. The directing of the tip plane cannot be based on tilting of the physical rotor axis, which is called the mast. Therefore, the tip plane and the mast are not perpendicular in forward flight, and each blade flaps up and down about the rotor hub during each revolution. Thus, in addition to a feathering hinge allowing control of blade angles collectively and cyclically, there must be a flapping

hinge at each blade root to allow vertical motion. The flapping hinge, seen in Fig. 2, is also necessary to relieve undesired aerodynamic rolling moments in forward flight by preventing bending moment differences at the blade roots from being transmitted through the rotor hub.
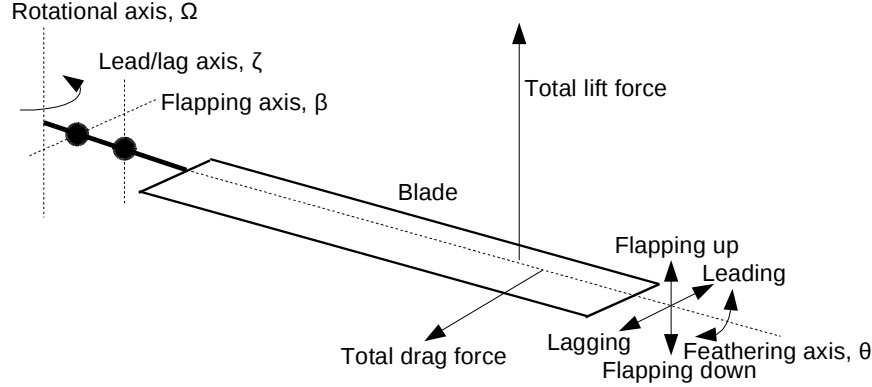

Figure 2. Three basic motions of a rotor blade rotating around the mast.

In a more general sense, the blade angles may also be controlled in such a manner that the thrust vector and the tip plane tilt laterally to generate a turning force for the helicopter. For any steady flight condition, the behavior of each blade angle $\boldsymbol{\theta}$ and the resulting flapping angle $\boldsymbol{\beta}$ with respect to the hub plane can be written as trigonometric functions of a rotational position $\boldsymbol{\Psi}$ from a selected reference as

$$\boldsymbol{\theta}(\Psi) = \boldsymbol{\theta}_0 - A_1 \cos \boldsymbol{\Psi} - B_1 \sin \boldsymbol{\Psi} \tag{1}$$

and

$$\boldsymbol{\beta}(\Psi) = \boldsymbol{\beta}_0 - a_1 \cos \boldsymbol{\Psi} - b_1 \sin \boldsymbol{\Psi} \tag{2}$$

The magnitude of the thrust is controlled by setting the constant or collective term $\boldsymbol{\theta}_0$, and the factors A_1 and B_1 define the magnitudes of the longitudinal and lateral cyclic control and thus the direction of the thrust vector. The collective control leads to a cone angle $\boldsymbol{\beta}_0$ for the flapping, and factors a_1 and b_1 describe the resulting flapping amplitudes caused by the cyclic control.

As a side effect of the flapping motion, another angular motion of the blades emerges. The angular momentum of each blade around the rotor mast tends to be conserved, but the radial distance of the center of gravity of a blade and the effective inertia vary due to the flapping. This means that the angular velocity of each blade varies during the rotation if its flapping angle is not constant. Thus, each blade performs oscillating motions in the rotating plane perpendicular to the mast, although in the tilted tip plane the rotation appears steady. To allow such a lead-lag movement $\boldsymbol{\zeta}$, another hinge at the blade root is needed. This completes the three basic motions of a single blade shown in Fig. 2 on top of the steady rotor rotation.

The actual construction of the rotor hub to allow control of the blade angles as well as the resulting flapping and the lead-lag motion varies greatly. In large modern helicopters like the UH-60A, all three angular motions are often combined in single elastomeric units forming effectively universal joints near the rotation axis at relative radial positions $e = r/R$. The hinge radius r is typically about 4 per cent of the rotor radius R.

Aerodynamic phenomena

In the hover, the rotor flowfield is, in principle, relatively simple. Without the actual helicopter fuselage and disregarding turbulence, the situation would be a steady state with a constant helical flowfield and a fixed rotor geometry. Each blade experiences the main relative inflow resulting from the rotor rotation, as illustrated in Fig. 3a, where the reference blade position $\mathbf{\Psi} = 0$ is thought to correspond to the location of the helicopter tail boom. The typical Mach numbers at the blade tips are approx. 0.6, meaning a subsonic flow. In practice, the fuselage causes flow disturbances that spoil the steadiness and regularity, but practical studies may still be conducted by assuming the idealized situation. In fact, the fuselage is actually completely omitted in most rotor simulations, even for more complex flying conditions. Also, the rotor hub can be neglected in the aerodynamic models.
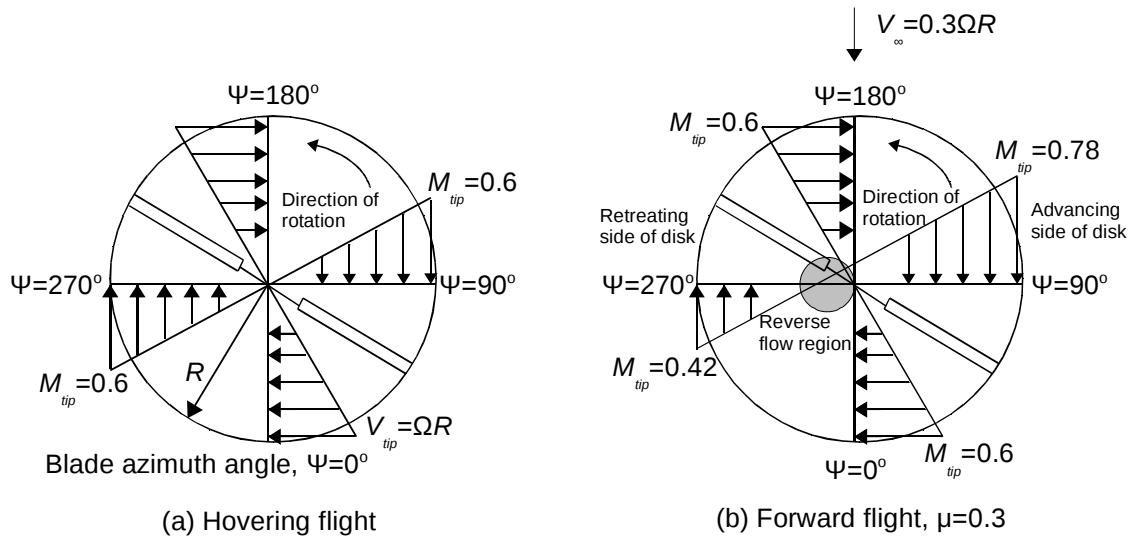

Figure 3. Main inflow experienced by rotor blades in a) hover b) forward flight.

In forward flight, the blade moving in the direction of flight on one side of the helicopter experiences a relative flow speed that is the sum of the linear flying speed and a radius-dependent component caused by the rotation, as shown in Fig. 3b. In contrast to the advancing blade, the retreating blade on the other side of the helicopter experiences only the difference of the linear and rotational velocity component. As the aerodynamic forces are proportional to the square of the relative flow velocity, the advancing blade tends to create a much higher force than the retreating blade. The forces are balanced by controlling the blades cyclically so that the relative angle between the blade airfoil and the local inflow, i.e. the angle of attack $\boldsymbol{\alpha}$, is much lower on the advancing side than on the retreating side.

Despite the cyclical blade angle control, high flying speeds are bound to cause aerodynamic problems for helicopter rotors. The local relative Mach numbers related to the advancing blade tip region grow so high that the flow becomes transonic with loss-producing shock waves and even shock-induced flow separation. In addition to the increase in blade drag, defined in Fig. 2, and the related power consumption, the lift producing the thrust is diminished and strong torsion moments may be induced in the blade. Simultaneously, the relative flow speed on the retreating side gets very low and even changes sign near the blade root. To produce useful lift, high blade angles and related angles of attack are

required, but eventually the flow would separate massively. During a rotor revolution, the flow conditions around each blade vary considerably and so quickly that the flow behaves clearly in a time-dependent manner. With increasing flying speed V, the flow problems with associated strong vibrations become severe. The advance ratio $\boldsymbol{\mu} = V/(\boldsymbol{\Omega}R)$ defines the extent of flow asymmetry, and helicopters are typically limited to flying below advance ratios of about 0.35.

In addition to the problems at high flying speeds, a potentially important source of aerodynamic vibration excitation is the interference of blades and the tip vortices trailing from the preceding blades. This phenomenon is the cause of the typical beating noise of helicopters. Especially when a helicopter is descending, the vortical rotor wake tends to interfere strongly with the blades.

Dynamic problems and simulations

As hinted above, vibrations are typical problems for helicopters. They are largely aerodynamically induced, but even slight differences in the structure or rigging between the blades are a source of strong vibrations. The centrifugal forces involved in large rotors rotating typically at around 250 RPM are very large, and the static and dynamic balancing of the blades must be conducted carefully. Naturally, it is also important that the blades remain in good shape both structurally and aerodynamically.

Until now in the discussion, the blades have been regarded as rigid bodies moving about the root hinges. In fact, real slender blades are very elastic, which makes the dynamics more challenging. The aerodynamic excitations cause elastic deformations at much higher frequencies than that corresponding to the rotor rotational speed. It must be checked that no resonances take place, but the torsional deformations of the blades may also cause significant modification of the aerodynamic loads by changing the effective angles of attack.

In detailed simulations of rotor dynamics, the blade elasticity must be taken into account, although certain studies can be conducted using a rigid-blade assumption. Even in such computations with three angular degrees of freedom for each blade, the large motion amplitudes must be properly modeled. For example, the flapping angles may be well over ten degrees, and the related movements of each blade section cannot be regarded as simple vertical translations. The geometrical non-linearity of the problem must be taken into account to produce the lead-lag motion.

The lead-lag motion is a problem itself because of its low natural damping. The flapping motion is inherently well damped because of the large related lift changes, but drag changes in the plane of rotation are small. In certain conditions on the ground, the lead-lag motion may even become unstable, and the resulting ground resonance may destroy the whole helicopter. Therefore, auxiliary damping for the lead-lag motion is required. This is accomplished by connecting a damper unit at the root of each blade. In addition to typically non-linear viscous damping, the units contain a spring that increases the natural frequency of the lead-lag motion. The damper units must, of course, be modeled in any rotor simulations even with rigid blades.

From the discussion above, it is evident that the simulation of a helicopter rotor in fast forward flight must combine a non-linear structural or mechanical model with a realistic time-dependent flow solver capable of modeling transonic effects and flow separation. Since only the blade pitch angles at their roots are actually controlled, there must be a genuine fluid-structure interaction to determine the blade motions and the related aerody-

namic forces. If the structural model is sufficiently detailed, such simulations can provide information about the vibration excitations at the hub and local blade loads related, for example, to blade repairs.

Modeling

Blade mechanics modeling

In the mechanical model of this study, the rotor blades are regarded as rigid bodies oscillating about their root hinges. Thus, the free blade motions are simulated by using two-degree-of-freedom (2-dof) moment equations for each blade. The variables to be solved in time are lagging (ζ) and flapping (β) angles, shown in Fig. 2. The applied equations are

$$\ddot{\beta} = \frac{-m(r_{cg} - eR)}{I_{\beta}} eR\Omega^2 \cos\zeta \sin\beta - \sin\beta\cos\beta(\Omega - \dot{\zeta})^2 + \frac{Q_{\beta}}{I_{\beta}} \tag{3}$$

and

$$\ddot{\zeta} = \frac{-m(r_{cg} - eR)}{I_{\zeta}\cos\beta} eR\Omega^2 \sin\zeta - 2\tan\beta(\Omega - \dot{\zeta})\dot{\beta} + \frac{Q_{\zeta}}{I_{\zeta}\cos^2\beta} \tag{4}$$

where m is the mass of the blade, r_{cg} is the distance between the center of gravity of the blade and the hub of the rotor, I_{β}, I_{ζ} are moments of inertia and Q_{β}, Q_{ζ} are external moments in the hinge point caused by aerodynamics and the spring-damping system.

In the simulations, the flow solver produces aerodynamic moments to be applied in the equations of motion. The spring-damping system associated with each blade is also modeled and the resulting moments are added in the 2-dof equations. In addition to the moments caused by aerodynamics and the damping system, centrifugal moments are included. The equations are solved by a fourth-order Runge-Kutta integration. Besides the attitude angles, the location of the blade (X, Y, Z) must also be calculated.

The third blade rotation that is the feathering angle, also seen in Fig. 2, is not a free variable. According to the desired rotor control, the feathering angle, i.e. the blade angle, is always predetermined by using Eq. 1. Besides the 2-dof equations, there is also an option to define all three angles as forced motions. This method (0-dof) can be utilized at the beginning of the simulation to avoid possible problems in the starting phase. In the 0-dof simulation, the flapping angle is calculated from Eq. 2 and the lagging angle remains constant.

It is well known that blade deformations are a significant factor in rotor operation. The elastic twist changes the local effective angles of attack, which in turn leads to marked modification of the blade and rotor loads. Therefore, the elastic twist must be taken into account at least in an approximate manner even in simulations where the blades are modeled as rigid bodies. In this study, the elastic deformation of the rotor in forward flight is modeled by simply adding a predefined extra term to the blade angle θ as a function of the rotation angle Ψ. For a hover case, the geometry of the blades is twisted beforehand.

Fluid mechanics modeling

For the fluid mechanics, a thin-layer approximation of the Navier-Stokes equations

$$\frac{\partial U}{\partial t} + \nabla \cdot (F - F_v) = Q(U) \tag{5}$$

Above $U = [\rho, \rho\vec{V}, \rho E]^T$ is a vector of the main variables, ρ the density, $\vec{V}$ the velocity, E the total energy consisting of enthalpy and kinetic energy. F is a vector of inviscid fluxes describing the pressure gradients and fluid convection, and viscous fluxes F_v contain the friction and turbulence effects. In the FINFLO code, source term $Q(U)$ is utilized to apply the interpolated values between overlapping grid blocks in the Chimera method [9].

For the time derivative in the present time-accurate solutions, a three-level fully implicit algorithm is applied [10]. Within each physical time step, the flow solution is updated by an implicit pseudo-time integration. For this, the LU-SGS method is applied in FINFLO with the Chimera technique. In order to accelerate the convergence, a multi-grid acceleration is employed, although it is not very effective in the time-dependent cases requiring short physical time steps.

For the convective fluxes, Roe's approximate Riemann solution is used. In the present case, a second-order TVD-discretization with the van Albada limiter is applied in a chord-wise direction and a third-order upwind-biased method in a wall-normal direction. In the radial direction, a second-order fully upwinded discretization is used. A central-difference method is employed for the viscous fluxes with the thin-layer approximation.

In the applied URANS technique, flow turbulence is taken into account by extra viscous flux terms and turbulent kinetic energy appearing in the time-averaged flow equations. In this study, Menter's $k - \omega$ SST turbulence model is utilized in all cases to produce the necessary turbulence parameters for the main flow equations. For simplicity, the flow is assumed to be fully turbulent, i.e. transition is not considered.

Performed simulations

UH-60A main rotor

The main purpose of this research is to validate the rotor simulation capability of the FINLFO flow solver. For the task, the main rotor of the Sikorsky UH-60A Black Hawk helicopter is selected as the test case. This geometry has been extensively studied, and results are given in many different publications, e.g. [1],[2],[3],[4],[6]. Besides experimental results, several simulations done by different research groups are described.

The UH-60A helicopter is equipped with a four-bladed rotor. Each blade is attached to the rotor hub by an elastomeric hinge, and there is an individual spring-damper unit for each blade. The geometry and dimensions of the blades are presented in Fig. 4. As indicated in Fig. 4, two different airfoil sections (SC1095 and SC1094 R8) are used in the UH-60A blade. The built-in radial twist of the blade chord line is given in Fig. 5. A positive twist raises the leading edge upwards and a negative value acts in the opposite way.

The coordinate system of the UH-60A rotor (X, Y, Z) in the FINFLO simulations is shown in Fig. 6. A free-stream velocity (V_∞) and direction parameters of the free stream, i.e. an angle of attack $(\boldsymbol{\alpha})$ and a nominal slideslip angle $(\boldsymbol{\beta})$, are also presented. The free-stream velocity corresponds to the flight speed V in Fig. 1. The rotor angular speed $(\boldsymbol{\Omega})$ is approximately 27.0 rad/s in this study, and rotation takes place around the Y-axis, as shown in Fig. 6. The radius of the rotor (R) is 8.18 m and the average chord length (c) is 0.528 m. The hinge points are located 0.381 m outwards from the rotor axis, corresponding to $e = 0.047$. The mass of each blade is 108 kg and the location of the center of gravity is 4.15 m outwards from the mast.
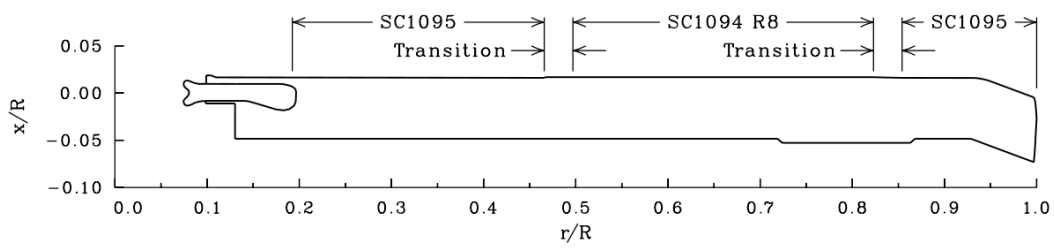
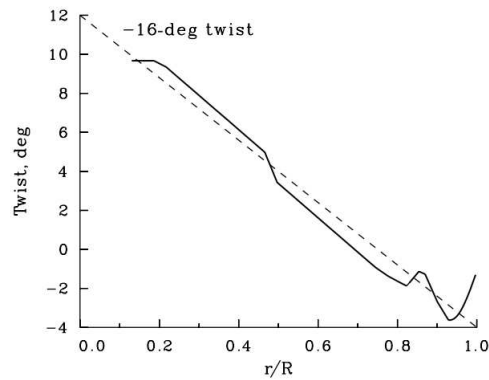Figure 4. The shape of the blade [11].
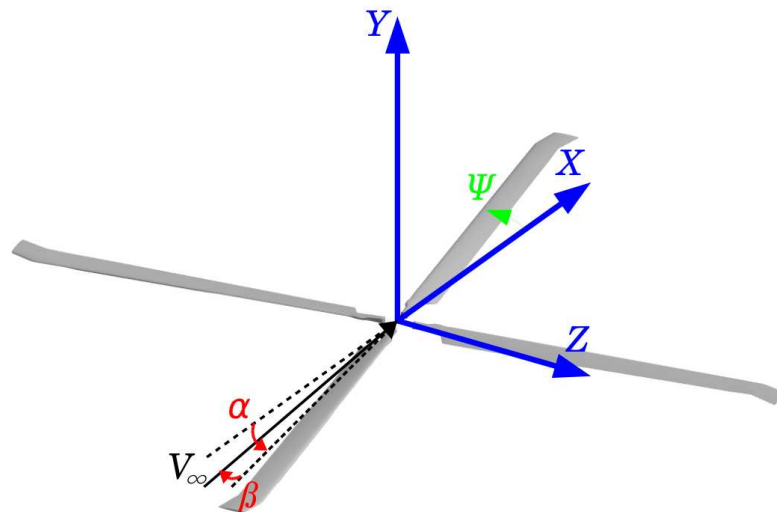

Figure 5. The geometric twist of the blade [11].

Figure 6. The coordinate system and flowfield parameters in the FINFLO simulations.

Simulation cases

Just two flight conditions are discussed in this paper. The first simulation is a hover case and the other one represents fast forward flight. The cases were selected so that two totally different situations will be treated. Another principle was to find flight conditions with comprehensive reference data. For the hover, direct reference data is available in Ref. [1]. For the forward flight, useful information can be found in [2],[3],[4],[6].

In the present idealized hover situation related to a wind tunnel test, the thrust force is to be zero. This value is not a practical case for an actual helicopter, but sufficient data for more representative hover cases were not found. With just the blades modeled, the situation is nominally a steady state. The simulation of the forward-flying rotor is equivalent to the flight test 8534 in NASA's research [6]. The free-stream velocity is fairly high and thus the advance ratio is μ=0.37. The operating conditions in this case are strongly time-dependent and this causes extreme challenges for computational modeling. Parameters for both simulation cases are presented in Table 1.

Table 1. Flight conditions and definitions of the rotor in simulation cases.

	Hover	Forward Flying
V_∞	0	80.37 m/s
ρ_∞	1.225 kg/m^3	1.225 kg/m^3
T_∞	288.15 K	288.15 K
α	0°	-7.31°
β	0°	1.28°
Ω	26.13 rad/s	26.7 rad/s
θ_0	0°	15.1°
A_1	0°	-4.89°
B_1	0°	7.63°

Computational grids

A mesh for the UH-60A rotor is generated in this study. Only the blades of the rotor are modeled and all other parts of the helicopter are neglected. In the grid system, four moving blade grids overlap a fixed background grid. The coupling between the grids is done by using the Chimera technique. A surface grid of the blade is shown in Fig. 7 and a close-up of the surface grid near the blade tip is drawn in Fig. 8. Since the most interesting phenomena in the flowfield occur close to the tip, the grid resolution is best here. In Fig. 4, there is a small tab at the trailing edge of the blade (approx. r/R=0.7...0.9), but the tab is not modeled in this study. The volume grid of the blade is depicted in Fig. 9. Each blade grid is split into four parts in order to facilitate parallel calculations. The total number of cells is 718 848 in one block, thus there are 2 875 392 cells for each blade. Simulations are usually started by using a coarser grid (a second or third grid level) obtained by omitting every second grid point from the original grid.
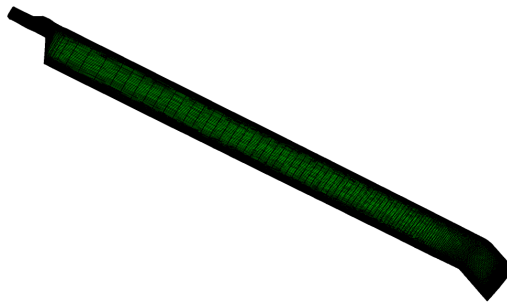

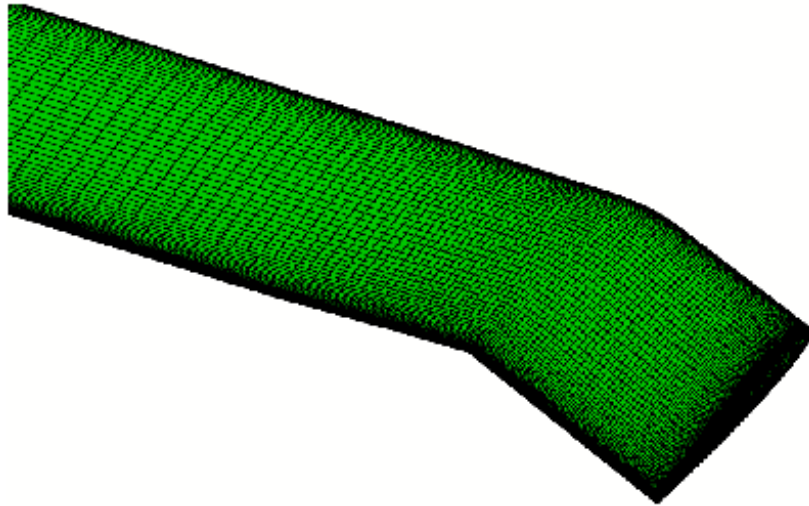Figure 7. Surface grid of the blade in the first grid level.

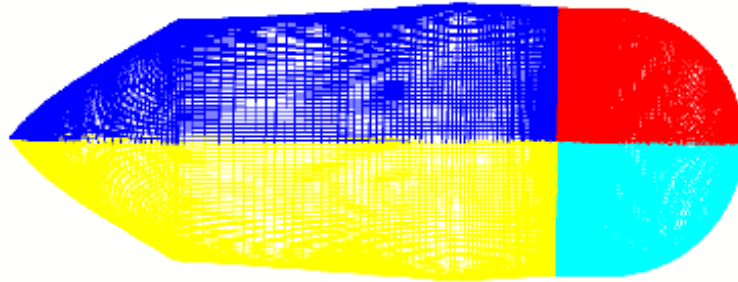Figure 8. Surface grid close to the blade tip in the first grid level.

Figure 9. Volume grid of the blade. The block division is shown by colors.

In the Chimera approach applied, a background grid is overset by the blade grids and the solution is interpolated between them. Different background grids are used in the hover case and the forward flying case. In both cases, the shape of the background grid is cubic. The background grid has to be sufficiently dense to capture the tip vortices accurately. For this purpose, there is a dense area in the middle of the grids. Because of the grid topology, the dense area also extends to the edges of the background grids. For parallelization, the background grids are also split into four parts. The total number of cells is 7 864 320 in the background grid for the hover and 14 155 776 in the background grid for the forward flight. Thus, the total number of computational cells is 19 365 888 in the hover case and 25 657 344 in the forward flight case. On the second-level grid the numbers are 2 420 736 and 3 207 168, respectively. The grid layout of the forward flying case is shown in Fig. 10. The background grid is tilted to locate the most accurate part of the grid in an area where tip vortices will emerge.

Boundary conditions on the external surface of the background grid are defined according to the free-stream values. On the external surface, where the flow is out from the computational area (bottom surface in the hover and surface behind the rotor in the forward flight), the pressure is defined from the free-stream values and the rest of the flow variables are extrapolated by the flow solver.
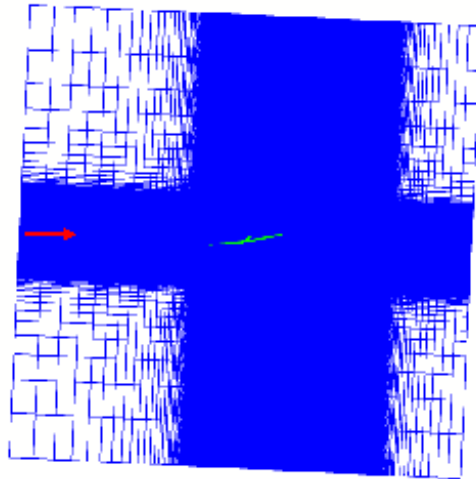
Figure 10. Volume grid in the forward flight conditions. The background grid is in blue and the surface grid of the blades is in green. A red arrow shows the direction of the free stream.

Computer runs

In the hover simulations at nominally zero thrust, the deformation of the blades was at first neglected and just the built-in shape was employed. After a few trials, it was confirmed that the deformation of the blade must be taken into account to obtain agreement with reference results. The geometric twist of the blade in the FINFLO simulations is presented in Fig. 11. The experimental result [1] is also plotted. It can be seen that the shape of the blade without the deformation deviates from the measured one, whereas the geometric twist applied in the final simulations is close to the actual one.
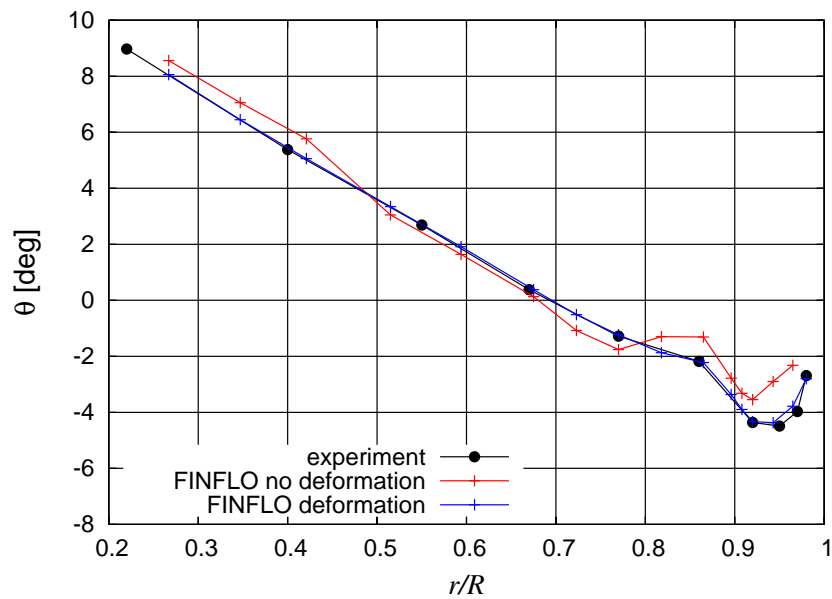
Figure 11. The geometric twist of the blade in the hover simulation conditions.

As the simulations were started, it was assumed that a steady-state fluid dynamics is an appropriate approach for the hover case. Later, it was noticed that the steady-state numerics produces an oscillatory solution. Thus, a time-accurate scheme was adopted for this case as well.

In the forward flight case, the elastic blade twist is modeled by adding a correction term $(\boldsymbol{\theta}_{\text{def}})$ to the nominal blade angle $\boldsymbol{\theta}$ as a function of the rotor rotation angle $\boldsymbol{\Psi}$. The correction actually related to a radial position of $r/R = 0.775$ is taken from Ref. [4] and it is shown in Fig. 12. With the rigid blades, the deformation correction is constant along the radius.
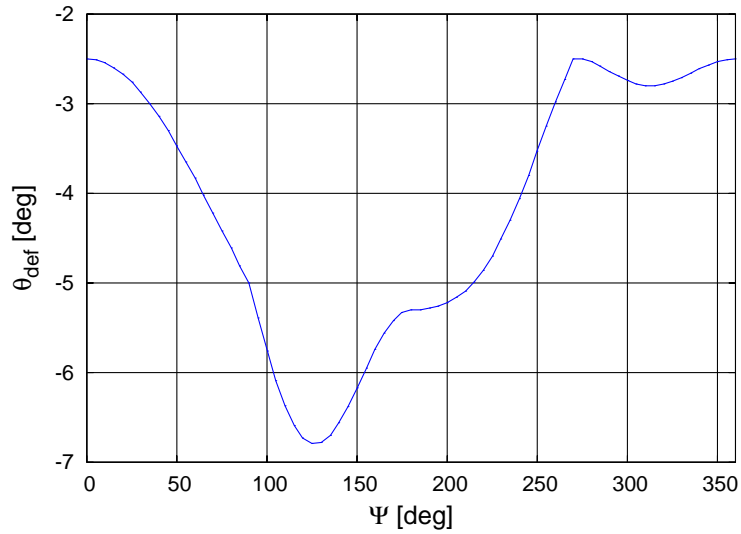
Figure 12. Deformation angle of the blade in the forward flight case. The deformation angle is presented as a function of the rotor angle.

The forward-flying rotor was simulated in different phases. At the beginning, the 0-dof scheme with completely predetermined motions was utilized. In the second phase, the 2-dof simulation was applied with initial blade control angles. The blade attitude angles during these two phases are shown in Fig. 13. In the next phase, the collective term of the blade angle $\boldsymbol{\theta}_0$ was adjusted to reach the desired thrust level. In addition to that, the flapping angle was trimmed to direct the thrust vector by editing the cyclic control. The flapping angle was compared with the references, and the simulation was continued with minor adjustments until a sufficient convergence was reached. In the final phase, the input data was kept constant and the simulation was continued long enough to store a time history of the rotor revolution. In order to save computing time, the first rotor revolution was simulated on the second grid level. After that the solution was interpolated onto the first grid level and the computation was continued for several revolutions.

In forward flight, the physical time steps applied were generally 0.001 seconds. This value corresponds to about 1.5 degrees of rotor rotation and 230 steps per revolution. The length of the steps and the number of internal iterations within steps were varied to ensure that the temporal accuracy is sufficient.
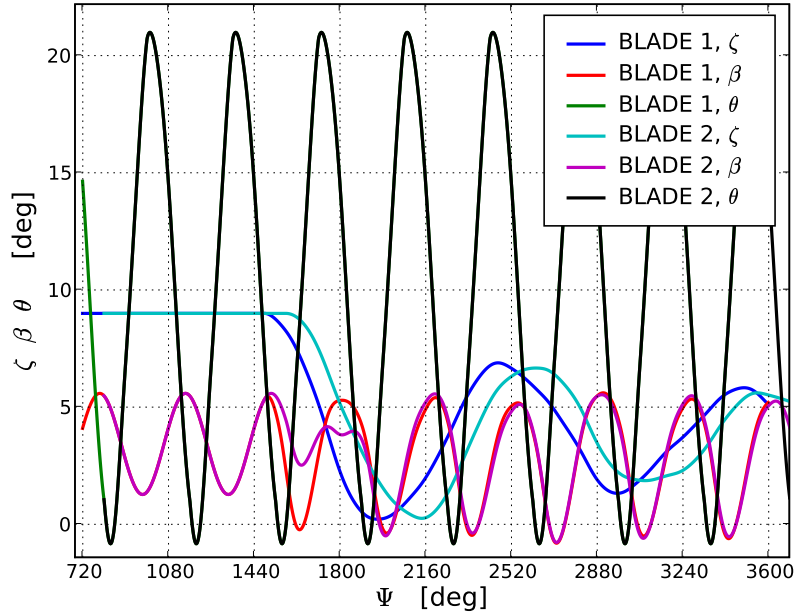
Figure 13. The attitude angles of blades 1 and 2 in the forward flying conditions.

Results for hover

As mentioned above, there were initial problems in the hover simulation. The main reason was the deformation of the blade, as seen in Fig. 14 that depicts computed and experimental radial thrust distributions in a non-dimensional form. For a major part of the radius, there is positive thrust according to the experiments, but close to the blade tips the thrust becomes clearly negative. Although the average values of the thrust computed with FINFLO without the deformation are close to zero, as desired, the distributions deviate markedly from the experimental results. In the simulation case where the deformation is taken into account, the correlation between the FINFLO result and the experimental result is considerably better. This comparison indicates the importance of the elastic twist even in rather trivial rotor simulations. The thrust distribution calculated by FINFLO still differs somewhat from the experiment, especially between sections r/R=0.6 and 0.85. The reason for this remaining small discrepancy probably lies in the inconsistencies in the definition of local airfoil chord directions between different references.

In the present case with zero overall thrust, the rotor does not produce strong axial flow through the rotor disc. This means that the wakes of the blades are bound to interfere with the following blades. Since the local thrust is seen to change sign at about $r/R = 0.87$, the trailing vortex pattern of the blades has two local extrema in the radial direction. The computed pattern is illustrated in Fig. 15, where a selected contour surface of flow vorticity colored by helicity is drawn. There is some vorticity around the blades, but the main features are the counter-rotating ring-shaped vortices related to the blade tips and to the location of the thrust reversal. FINFLO is able to simulate the tip vortices and these exist through the grid block boundaries. The location of the vortices is similar to that found in Ref. [1].

In addition to the radial force distributions and global flow patterns, the chordwise pressure distributions at various blade sections were studied. Results for one such section at r/R=0.945 are shown in Fig. 16. The non-dimensional pressure on the upper and lower side of the section computed with FINFLO is given in blue, whereas the background shows computational and experimental results taken directly from Ref. [1]. Despite the poor quality of the reference figure, it is seen that the current results obtained with the deformed blade shapes agree well with the experiments and the best reference calculations.

The achieved total thrust force is just about 2000 N, which is very small in comparison with representative weights of the UH-60A. Despite this desired thrust level, some oscillations remain in the solution even after computer runs corresponding to 18 rotor revolutions. Obviously, the mild flow case takes a very long time to converge completely.
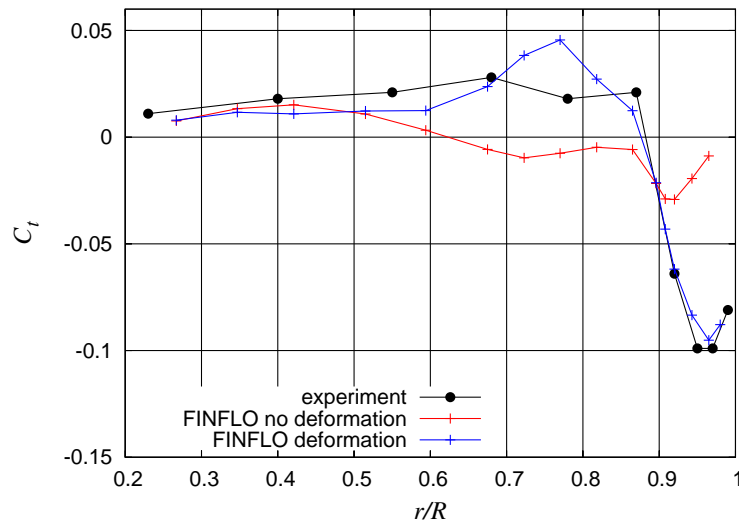

Figure 14. Radial thrust distributions in a non-dimensional form for the hover at zero thrust. The experiment result is from Ref. [1]. FINFLO results are presented with and without deformation.
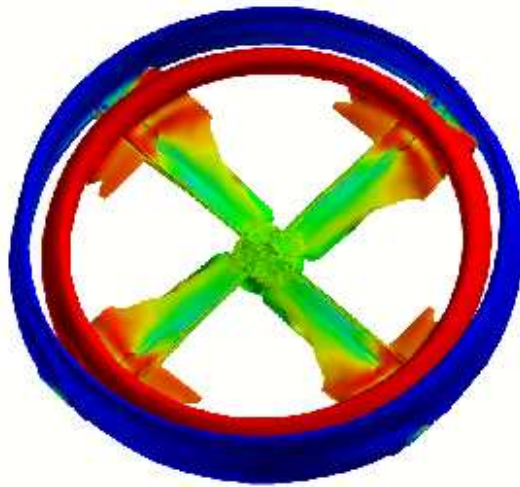

Figure 15. A selected iso-surface of computed flow vorticity colored by helicity in the hover at zero thrust. Red and blue refer to the counter-rotation of trailing vortices.
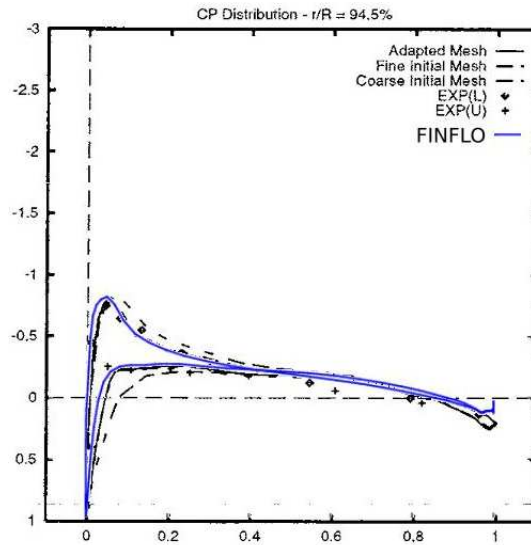
Figure 16. Non-dimensional chordwise pressure distributions at section $r/R = 0,945$ in the hover. The FINFLO result is added afterwards to the original picture of Ref. [1].

Results for forward flight

The evolution of the aerodynamic forces and moments of the rotor in forward flying conditions are shown in Fig. 17. The simulation contains several phases, and in these graphs only a short period of the simulation is presented. It can be noticed that all the components are time-dependent. The adjustments of the blade angle can be seen as sharp peaks in the curves. The overall trend of the curves demonstrates that a final periodic state has been reached. The most interesting value is the axial force FY_a that corresponds essentially to the thrust. A reference for the thrust coefficient history is given in Refs. [2] and [3], from which a dimensional reference force of 85 kN is obtained. It can be seen in Fig. 17 that a correct level of thrust is achieved.

The flap angle of each blade during one rotor revolution is shown in Fig. 18. The general agreement between the FINFLO curve and references is fair. The deformation model in the FINFLO simulations is primitive and this is the main cause of discrepancy. It would be possible to adjust the blade angle during the FINFLO simulations to shift the flap angle closer to the references. However, in addition to the flap angle the thrust vector (Fig. 17) must also be correlate well with the references. As a compromise is made between the averaged thrust and the blade behavior, the result of the flap angle in the FINFLO simulations is not as good as it could be.

The downwash velocity below the rotor is visualized in Fig. 19. It can be easily seen that the flowfield is highly asymmetric. In addition, the flowfield is strongly time-dependent. On the advancing side of the rotor, there is a strong downwash in the root area of the blade. The blade on the retreating side of the rotor generates downwash in the tip area of the blade. There is a small area where the flowfield is in an upwash condition close to the root of the blade on the retreating side of the rotor. The flowfield convects as the wake of the rotor and the gradients weaken while the wake is aging.

The vorticity structure below and behind the rotor is visualized in Fig. 20. There are strong vorticity tubes behind the tip area of the blades on the advancing and retreating sides of the rotor. These vortical areas are periodically connected by tip vortices. There is also an additional vorticity tube close to the hub of the rotor produced by all of the blades.

200

The vorticity structure in the FINFLO simulations contains elements from approximately five rotor revolutions. This suggests that the turbulence modeling is working properly without causing excessive dissipation. The vorticity structure also verifies that the grid resolution is adequate.

Local normal force and pitching moment coefficients during one rotor revolution are shown in Fig. 21. There are curves at three different blade sections. In every section, there are flight test values (c8534) and two reference simulation results in addition to the FINFLO curves. Considering the highly dynamic nature of the solution, the FINFLO results are in good agreement with the other sets. There are differences between all of the curves, but the FINFLO results do not deviate from the other results. As the deformation modeling in the FINFLO simulations is greatly simplified compared to the references, the present results can be regarded as good.

Finally, comparisons of the time-averaged radial normal force distributions are made in Fig. 22. FINFLO is seen to overestimate the normal force in the blade tip area and underestimate it in the root area. The radially constant blade deformation angle applied in the FINFLO simulation (see Chapter) is obviously responsible for this discrepancy, as the correction is correct at section $r/R = 0.775$. The deformation towards the tip of the blade is too small. On the other hand, the deformation correction in the FINFLO simulation is excessive in the root area, where the elastic torsion should actually vanish at the blade hinge.
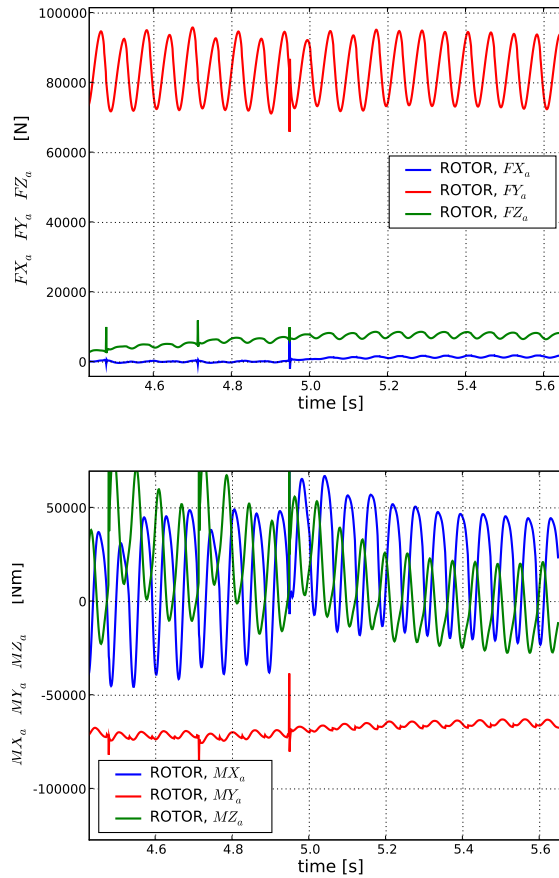

Figure 17. Rotor aerodynamic forces (upper) and moments (lower) in the forward flying conditions. The coordinate system is presented in Fig. 6
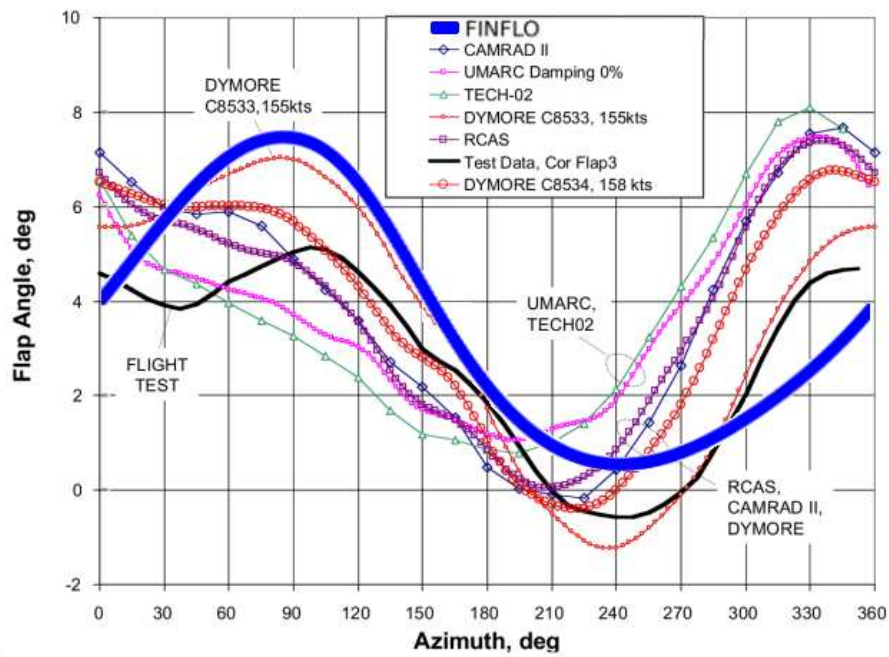
.

Figure 18. Flap angle as a function of a rotor angle in the forward flying conditions. The FINFLO result is added afterwards to the picture of Ref. [7].
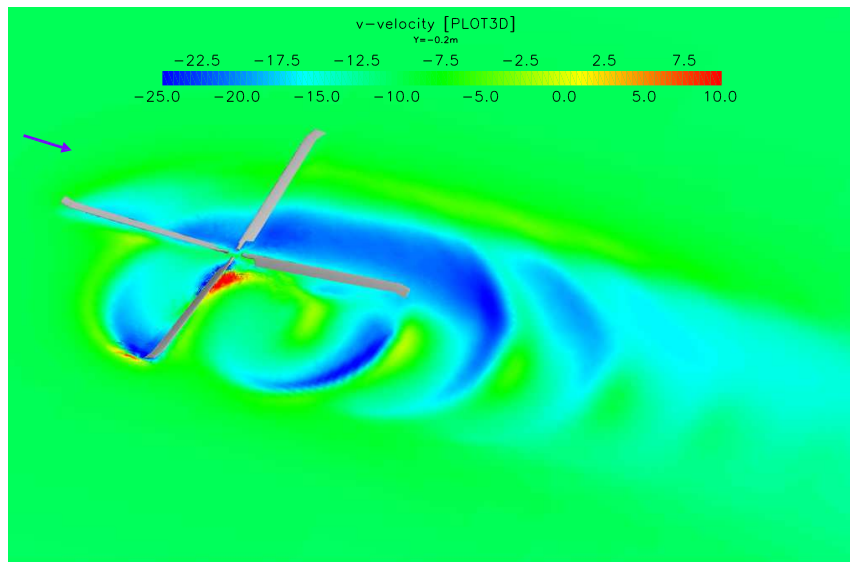

Figure 19. Downwash velocity (flow velocity perpendicular to the plane of rotation) 0.2 m below the hub of the rotor in the forward flying conditions. The free-stream direction is shown by a purple arrow.
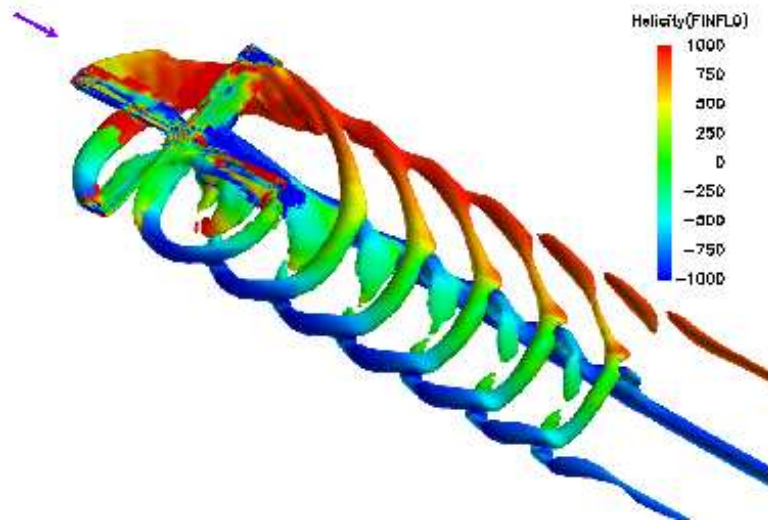
Figure 20. A selected iso-surface of computed flow vorticity colored by helicity in the forward flying conditions. The free-stream direction is shown by a purple arrow.
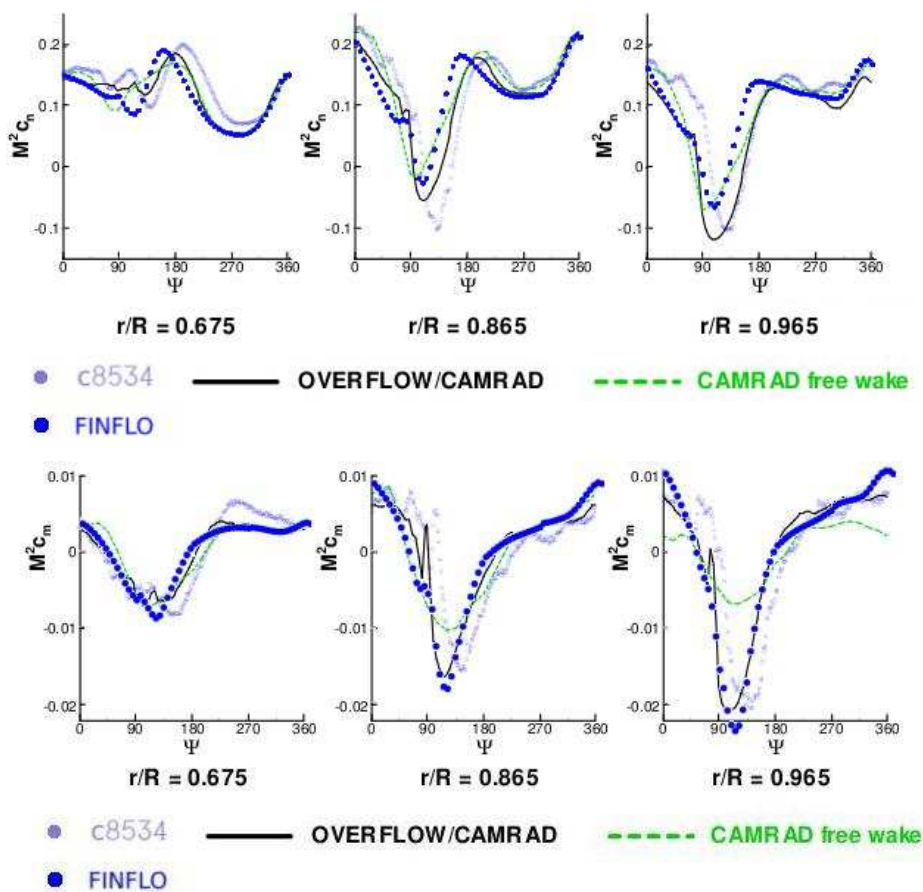

Figure 21. Normal force coefficient (upper) and pitching moment coefficient (lower) as a function of rotor angle in the forward flying conditions. The FINFLO results are added afterwards to the picture found in Ref. [2].
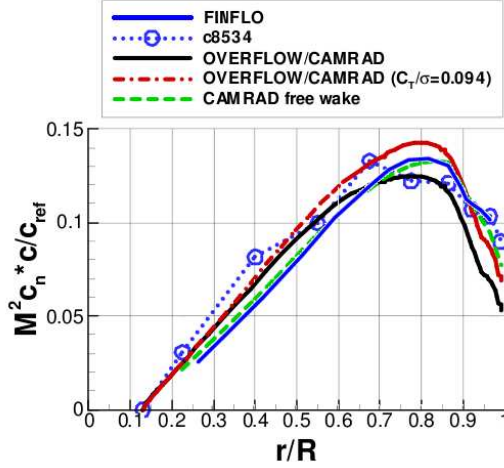
Figure 22. Mean normal force distribution in the forward flying conditions. The FINFLO result is added afterwards to the picture found in Ref. [2].

Conclusions

In this work, the flowfield around the main rotor of the UH-60A helicopter was computed in order to validate the FINFLO flow solver for other rotor studies. The four blades were considered to be rigid, and 2-dof equations were utilized to simulate their mechanical behavior about the root hinges. The flow simulations were based on Reynolds-averaged Navier-Stokes equations solved in a time-accurate manner using a Chimera grid, and the flow turbulence was modeled by the well-established $k - \omega$ SST turbulence model. Two operating conditions were studied: hover at zero thrust and forward flight at high speed. These flight conditions were selected so that appropriate experimental and computational reference results would be available.

It was clearly seen that the blade deformations play a key role in the helicopter rotor flow simulations. The initial simulation results without any deformations were in poor correlation compared to the reference results. Thus, the elastic twist was taken into account during further simulations by simplified methods. In the hover case, the deformation could be applied beforehand and during the simulation run no correction was needed. In forward flight, the deformation was taken into account by adding an extra term dynamically to the blade setting angle. With these deformation models, the FINFLO flow solver produced results which are generally in good correlation compared to the reference data.

Despite the incomplete deformation modeling that is bound to cause some inaccuracies, it could be demonstrated that the FINFLO flow solver is able to simulate the flowfield of a helicopter rotor in a realistic manner. The performed simulations with highly dynamic fluid-structure interaction can be regarded as quite demanding, and the eventual success of the work with limited resources was not assured. In the future, the mechanical behavior of the rotor should be modeled in a more sophisticated manner with a real, non-linear structural model. The flow simulation itself might be performed more accurate by using detached-eddy simulation (DES), and also transition modeling in the boundary layer would bring more accuracy.

Acknowledgements

References

[1] M. Dinar, A. Leminos and M. Shephard. *Adaptive Solution Procedures for Rotorcraft Aerodynamics.* Rensselaer Polytechnic Institute, Rotorcraft Technology Center, Troy, NY, USA, 1997.

[2] M. Potsdam, H. Yeo and W. Johnson *Rotor Airloads Prediction Using Loose Aerodynamical/Structural Coupling.* American Helicopter Society 60th Annual Forum, Army/NASA Rotorcraft Division Aeroflightdynamics Cirectorate (AMRDEC) U.S. Army Research, Development, and Engineering Command, Moffett Field, CA, USA, 2004.

[3] M. Potsdam, H. Yeo and W. Johnson. Rotor Airloads Prediction Using Loose Aerodynamical/Structural Coupling. *Journal of Aircraft* 3(43):732 - 742,2006.

[4] A. Datta. *Fundamental Understanding, Prediction and Validation of Rotor Vibratory Loads in Stedy Level Flight.* Doctoral Thesis, University of Maryland, College Park, MD, USA, 2004.

[5] P. F. Lorber. *Aerodynamic Result of a Pressure-Instrumented Model Rotor Test at the DNW.* United Technologies Research Center East Hartford, Conn., USA, 1991.

[6] www pages. UH-60 Airloads Program Tutorial. *http://rotorcraft.arc.nasa.gov/tutorial/index.html#0.* 2011

[7] H. Pomin and W. Siegfriend *NRTC/RITA Rotorcraft Airloads Workshop, UH-60 Rotor Airloads/Blade Load - Comments.* Stanford University, Moffett Field, CA, USA, Aug. 31 - Sept. 1 2004.

[8] T. Siikonen, J. Hoffren and S. Laine. *A Multigrid LU Factorization Scheme for the Thin-Layer Navier–Stokes Equations.* Proceedings of the 17th ICAS Congress, pp. 2023-2034, ICAS Paper 90-6.10.3, Stockholm, Sept., 1990.

[9] T. Siikonen, P. Rautaheimo and E. Salminen. *Numerical Techniques for Complex Aeronautical Flows* Proceedings of the ECCOMAS 2000 Conference, Barcelona, Sept., 2000.

[10] J. Hoffren, T. Siikonen and S. Laine. Conservative Multiblock Navier-Stokes Solver for Arbitrarily Deforming Geometries. *Journal of Aircraft* 6(32):1342–1350,1995.

[11] W. G. Bousman. *Aerodynamic Characteristics of SC1095 and SC1094 R8 Airfoils.* NASA TP-2003-212265, Aeroflightdynamics Directorate U.S. Army Research, Development, and Engineering Command Ames Research Center Moffett Field, CA, USA, 2003

Juho Ilkko
Finflo Ltd.
Tekniikantie 12, 02150 Espoo, Finland
`juho.ilkko@finflo.fi`

Jaakko Hoffren
Patria Aviation Ltd.
Naulakatu 1, Tampere, Finland
`jaakko.hoffren@patria.fi`

Timo Siikonen
Aalto University School of Engineering
02015 Aalto, Finland
`timo.siikonen@aalto.fi`